Photonic spin-controlled self-hybridized exciton-polaritons in WS$_2$ metasurfaces driven by chiral quasibound states in the continuum

Hongmiao Zhou,[1,*] Meng Qin,[1,*] Hangsheng Xu,[1] Gangao Wei,[1] Hongju Li [1,†]
Weiqing Gao [1,‡] Jianqiang Liu,[2] and Feng Wu[3]

[1]*School of Physics, Hefei University of Technology, Hefei, Anhui 230009, China*
[2]*School of Science, Jiujiang University, Jiujiang 332005, China*
[3]*School of Optoelectronic Engineering, Guangdong Polytechnic Normal University, Guangzhou 510665, China*

Bulk transition metal dichalcogenides (TMDs) have found widespread applications on nanophotonics, condensed matter physics, and quantum optics, due to their high refractive index and stable excitonic response at room temperature. In this paper, based on the finite-element method simulations, we demonstrate that the high refractive index enables the fabrication of bulk WS$_2$ into high-quality-factor metasurfaces that support chiral quasibound states in the continuum (Q-BICs). Interestingly, the Q-BIC resonance can in turn hybridize with excitons in the WS$_2$ metasurface itself. The self-hybridized exciton-polaritons, induced by the strong coupling between a Q-BIC and excitons, exhibit a typical anticrossing behavior with the Rabi splitting up to 136.5 meV. Such remarkable anticrossing behavior is also well elucidated by the coupled oscillator model. Intriguingly, we numerically verify that the self-hybridized exciton-polaritons are photonic spin-controlled, attributed to the chiral Q-BIC with the circular dichroism approaching 0.91. Therefore, we can control the exciton-photon interaction by simply changing the helicity of incident light. We believe that the outstanding self-hybridized exciton-polaritons in a WS$_2$ metasurface itself, without external microcavities, could pave the way for large-scale, low-cost integrated polaritonic devices at room temperature. Additionally, the chiral Q-BIC will enrich the toolbox for engineering exciton-photon interactions in bulk TMDs and other semiconductors. The photonic spin-controlled self-hybridized exciton-polaritons would find utility in ultrafast all-optical switches, modulators, chiral light-emitting devices, and valleytronic devices.

I. INTRODUCTION

Exciton-polaritons, a prototypical form of light-matter interaction, arise from the strong coupling between semiconductor excitons and photons within microcavities [1]. As half-light, half-matter bosons, exciton-polaritons exhibit favorable characteristics including low effective mass, fast propagation, and strong nonlinearity [2,3]. These attributes enable exciton-polaritons to play significant roles in not only fundamental sciences but also novel optoelectronic and quantum applications such as quantum entanglement [4], Bose-Einstein condensation [5], low-threshold lasing [6], and all-optical circuits [7]. The experimental exploration of exciton-polaritons can trace back to the GaAs and CdTe planar quantum wells [8,9]. However, because of their small exciton binding energies (about 4 meV for GaAs and 10 meV for CdTe) [10,11], the exciton-polaritons in the GaAs or CdTe systems exist only at cryogenic temperature, e.g. 5 K. Constrained by the cryogenic temperature, the exploration of novel systems capable of sustaining room-temperature exciton-polaritons has garnered increasing interest in recent

decades. The semiconductor systems with a large exciton binding energy against room temperature thermal fluctuation (the corresponding thermal excitation energy is $k_B T \approx$ 26 meV, where k_B is the Boltzmann constant, and $T = 300$ K is the temperature) have been considered as promising candidates. To date, the ZnO, GaN, organic semiconductors, halide perovskites, and monolayer transition metal dichalcogenides (TMDs) have been reported to facilitate substantial experimental progress in the realm of room-temperature exciton-polaritons [12]. Among these semiconductors, direct band gap monolayer TMDs have received enormous attention. The excitons in monolayer TMDs exhibit a small Bohr radius of a few nanometers. In combination with the two-dimensional quantum confinement and significantly suppressed dielectric screening, the Coulomb interaction in monolayer TMDs is greatly enhanced, leading to the excitons with a large oscillator strength and a high binding energy over 300 meV (e.g., 320 meV for WS$_2$, 500 meV for MoS$_2$, 550 meV for MoSe$_2$, 370 meV for WSe$_2$) [13–16]. The various microcavities including photonic crystals, metamaterials, planar microcavities enabled by distributed Bragg reflectors, and plasmonic metallic nanoparticles, have been proposed for strong coupling with monolayer TMDs [17–22]. Consequently, the room-temperature exciton-polaritons with the Rabi splitting energy approaching 300 meV have been successfully achieved [23]. Nevertheless, the use of external

---
*These authors contributed equally to this work.
†hjli@hfut.edu.cn
‡gaoweiqing@hfut.edu.cn

microcavities alongside adjacent monolayer TMDs inevitably imposes limitations related to strain, mode overlap, and material integration, making it impractical for designing ultracompact polaritonic devices. Therefore, for the fabrication of ultracompact polaritonic devices, it is highly desirable for room-temperature excitonic materials themselves to serve as resonant microcavities, realizing self-hybridized exciton-polaritons without the need for a separate microcavity to confine the field.

Fortunately, bulk TMDs host stable excitons at room temperature and simultaneously exhibit a high refractive index in the visible range [24]. The high refractive index will facilitate strong light confinement in patterned bulk TMDs through geometric resonances, determined by oscillation of induced polarization charges or displacement currents. Specifically, only utilizing bulk TMD platforms enables the integration of a resonant microcavity and excitonic materials into a single nanostructured system, making the realization of self-hybridized exciton-polaritons feasible [25]. To date, the nanopatterned bulk TMDs have been reported to support various microcavity resonances such as Fabry-Pérot resonances, surface lattice resonances, guided-mode resonances, and Mie resonances [26–30]. When the energy of these resonances is tuned across the TMD excitons, the nontrivial anticrossing behavior with a large Rabi splitting energy is observed, which thus affirms the occurrence of self-hybridized exciton-polaritons induced by the strong coupling between the resonant microcavity and the exciton itself [28,30]. In general, the coupling strength between excitons and resonant microcavities depends on the inner product of the electric field E in the resonant cavity and the exciton transition dipole moment μ_e of bulk TMDs. In the passive self-hybridizing structures, the coupling strength is determined by the ratio of the quality factor (Q factor) to the mode volume (V) of the resonant cavity [31]. Therefore, achieving a high Q factor in TMD resonant cavities is crucial to observing a remarkable anticrossing pattern with a larger Rabi splitting energy. Recently, the design of resonant microcavities using bound states in the continuum (BICs) has gained significant attention, owing to the unbounded Q factor and strong field confinement simultaneously [32–34]. Ideal BICs, as nonradiating eigenvalues, are spectrally invisible and inaccessible externally, preventing them from hybridizing with excitons. Fortunately, the small perturbation in the geometrical parameter will enable BICs to transform into externally accessible quasi-BICs (Q-BICs) [35–37], which still possess ultrahigh Q factors and strong field enhancement. Therefore, the bulk TMD nanostructures governed by Q-BICs [38] have become the ideal platform for investigating self-hybridized exciton-polaritons. The bulk TMDs have been designed into asymmetric rod-type metasurfaces, elliptical metasurfaces, slotted gratings, and nanodisk metasurfaces, to facilitate the Q-BICs [39–43]. Consequently, the ultrastrong coupling between a Q-BIC and the exciton itself has been witnessed, leading to the self-hybridized exciton-polaritons with the Rabi splitting energy larger than 200 meV [43]. However, in the mentioned Q-BIC driven bulk TMD systems, the methods to control exciton-photon interaction are limited, with most relying on passive changes in geometric parameters. Importantly, the reports of self-hybridized exciton-polaritons based on a chiral Q-BIC
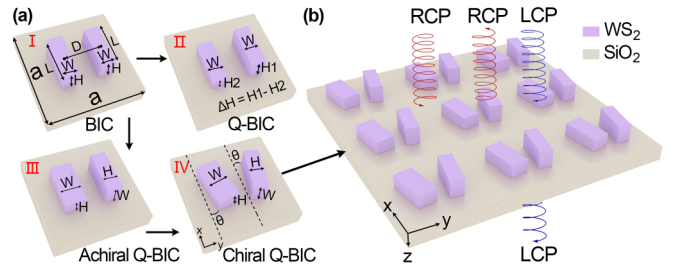

FIG. 1. (a) Square unit cell of a bulk WS$_2$ metasurface with a pair of parallel and identical rectangular nanobars is marked by the pattern I, which is designed for exciting the symmetry-protected BIC. Only the change in the height difference (ΔH) of two nanobars allows the symmetry-protected BIC to transform into a Q-BIC, corresponding to the pattern II. The pattern III describes the parallel nanobars with $W \neq H$, but one nanobar is turned on its side. It is used for exciting an achiral Q-BIC. When the nanobars in pattern III are further diverged by an in-plane rotation, the maximum chiral Q-BIC is possible for the pattern IV. In the pattern IV, the nanobars are rotated in-plane around their respective centers. The tilt angle is defined by the θ between the x axis and the long axis of the nanobar. (b) Schematic of the chiral Q-BIC driven bulk WS$_2$ metasurface under the illumination of circularly polarized lights.

[44–47] on bulk TMD metasurfaces are rare. The chiral Q-BIC will further offer a new opportunity to actively control exciton-photon interaction only by adjusting the helicity of the incident light.

In this paper, we numerically investigate a bulk WS$_2$ metasurface consisting of a pair of parallel and identical nanobars. Finite-element method simulations suggest that it supports a symmetry-protected BIC driven by a pair of antiparallel electric dipoles. When one nanobar is turned on its side and two nanobars are tilted, the maximum chiral Q-BIC resonance is observed. By changing the lengths of nanobars, the Q-BIC resonance is tuned across the WS$_2$ A exciton. The outstanding anticrossing behavior, with a Rabi splitting energy up to 136.5 meV, is observed and theoretically demonstrated by the coupled oscillator model. Thus, the self-hybridized exciton-polaritons induced by the strong coupling between a Q-BIC and excitons itself are achieved as expected. Intriguingly, the self-hybridized exciton-polaritons are verified to be photonic spin-controlled, attributed to the chiral Q-BIC with the circular dichroism approaching 0.91. Hence, we can dynamically switch the exciton-photon interaction by simply varying the helicity of incident circularly polarized light. We believe that the remarkable self-hybridized exciton-polaritons in WS$_2$ metasurfaces without external microcavities are not only of fundamental interest but could also pave the way toward large-scale and low-cost integrated polaritonic devices for quantum and nanophotonic applications. The chiral Q-BIC scheme undeniably provide a new degree of freedom for dynamically modulating the exciton-photon interaction on other TMD materials and perovskites.

II. GEOMETRIC STRUCTURE AND NUMERICAL MODEL

Figure 1(a) shows the geometric transformation of the bulk WS$_2$ metasurface unit cell, to illustrate the evolution of a symmetry-protected BIC to the maximum chiral Q-BIC. We

choose the WS_2 for the realization of our Q-BIC metasurface, due to the highest refractive index exceeding 4.5 in the visible range [24]. The high refractive index enables the Q-BIC resonance in smaller size metasurfaces, thereby benefiting densely packed exciton-polaritons systems. Additionally, compared to other TMDs (MoS_2, $MoSe_2$, and WSe_2), WS_2 exhibits a larger difference between A and B exciton transition energies, resulting in a spectrally isolated A exciton at 621 nm. Thus, we can eliminate the influence of other excitons and focus solely on the coupling between the A exciton and the Q-BIC resonance. Importantly, a significant advantage, when compared with other TMDs, is that WS_2 exhibits a large ratio of exciton oscillator strength to line width at room temperature, making it more suitable for achieving noticeably exciton-polaritons induced by the strong coupling.

The metasurface unit cell comprises paired rectangular WS_2 nanobars. The unit cell consisting of two parallel and identical nanobars is marked by the pattern I, where the length of nanobars is denoted as L, the width as W, the height as H, the period as a for both x and y directions. The distance between centers of mass of two nanobars is marked by D. For the pattern I, the metasurface maintains the C_2^z symmetry (π rotational symmetry around the z axis) and the σ_z symmetry (the up-down mirror symmetry along the z direction) simultaneously, which are sufficient to support a symmetry-protected BIC in theory [48,49]. To open the radiation channel of the potential symmetry-protected BIC, thereby obtaining the externally accessible Q-BIC, we break the out-of-plane symmetry of the metasurface by changing the height difference between two nanobars [50], as indicated by the pattern II. To create the maximum chiral Q-BIC, we first consider the achiral Q-BIC on the pattern III, where the parallel nanobars have equal footprints but one of which is turned on its side. Then, we investigate the chiral Q-BIC on the pattern IV, where both bars further diverge with an opening angle of θ [51–53]. The periodic array of a WS_2 metasurface with the unit cell formed by the pattern IV is shown in Fig. 1(b).

Firstly, the eigenmodes of the bulk WS_2 metasurface with the unit cell formed by the pattern I are investigated. The geometric parameters are selected as $a = 280$ nm, $L = 155$ nm, $W = 63$ nm, $H = 84$ nm, and $D = 140$ nm. The dielectric function of the bulk WS_2 is determined by the classical Lorentzian oscillator [25,27,43]

$$\varepsilon(\omega) = \varepsilon_B + \frac{f_0 \omega_{ex}^2}{\omega_{ex}^2 - \omega^2 - i\omega\gamma_{ex}}. \quad (1)$$

Here, $\varepsilon_B = 20$ is the background permittivity dominated by higher energy transitions. The $\hbar\omega_{ex} = 2.0$ eV represents the A exciton transition energy and the $\hbar\gamma_{ex} = 50$ meV denotes the exciton full line width. The f_0 stands for the exciton oscillator strength. To characterize the resonant properties of the bulk WS_2 metasurface microcavity, the background index-only material is considered and thus the oscillator strength is set to $f_0 = 0$. For the subsequent investigation of self-hybridized exciton-polaritons on bulk WS_2 metasurface, we set the oscillator strength to $f_0 = 0.2$. In the implementation, the eigenfrequency solver in COMSOL Multiphysics 5.6 is utilized to calculate the eigenmodes. The Floquet periodic boundary conditions are applied in the x and y directions to determine the in-plane wave vectors ($k_x = k_y = 2\pi/a$), and

the perfectly matched layers are used in the z direction to absorb the radiation wave. To minimize the background reflections, the WS_2 metasurface supported by a transparent silica substrate should be covered by a same transparent dielectric. In our simulations, we immerse the WS_2 nanobars in a transparent uniform dielectric background with the refractive index of 1.5 for simplicity. To select the transverse electric eigenstates, a perfect magnetic conductor as a boundary condition is set at the middle of the WS_2 metasurface. The first Brillouin zone of a square lattice is schematically shown in the inset of Fig. S2(a) of the Supplemental Material [54]. The calculated complex eigenfrequencies are expressed by $\omega_0 = f + j\eta$, in which the real part (f) is the resonance frequency and the imaginary part (η) represents the leakage rate. The Q factor of the eigenvalue is defined as $Q = \frac{1}{2}\frac{\text{Re}(\omega_0)}{\text{Im}(\omega_0)} = \frac{f}{2\eta}$. The selective band structure in the visible range is in Fig. S2(a) of the Supplemental Material [54] and the corresponding radiative Q factors are presented in Fig. S2(b) of the Supplemental Material [54].

III. SIMULATION AND DISCUSSION

The results from the eigenvalue calculations (see Figs. S1 to S4 of the Supplemental Material [54]) suggest that the WS_2 metasurface with the unit cell formed by the pattern I supports a symmetry-protected BIC carrying a topological charge of $q = -1$. Meanwhile, this BIC is dominated by a pair of antiparallel electric dipoles on nanobars. Owing to the symmetry mismatch between the mode profile of this BIC and that of the external propagating wave, the observed BIC cannot be excited by any linearly polarized plane waves under normal incidence [55–60]. The coupling between the eigenmode of the metasurface with the unit cell formed by the pattern I and the far field can be described by the parameter m_e [61]

$$m_e \propto p_1 \cdot e e^{ikz_1} + p_2 \cdot e e^{ikz_2}, \quad (2)$$

The $\mathbf{p}_{1,2}$ are the electric dipole moments of two nanobars and $z_{1,2}$ are their effective z coordinates. The $\mathbf{e}$ is the unit vector of the polarization of a plane wave propagating along z direction and with the wave vector $\mathbf{k}$. For the BIC resonance on paired parallel and identical nanobars [the pattern I in Fig. 1(a)], a pair of antiparallel electric dipoles are along the x axis (see Fig. S2(c) of the Supplemental Material [54]). The antiparallel electric dipoles have same magnitudes ($|\mathbf{p}_1| = |\mathbf{p}_2|$) and the effective z coordinates. Thus, the $\mathbf{p}_1 = -\mathbf{p}_2$ and $z_1 = z_2$ enable the BIC with $m_e = 0$. To open the radiation channel of the symmetry-protected BIC and transform it into an externally accessible Q-BIC, we reduce the height of one nanobar. The small height difference (ΔH) will give rise to $\mathbf{p}_1 \neq -\mathbf{p}_2$ and $z_1 \neq z_2$. Therefore, for the pattern II, the nanobars with different heights will support antiparallel electric dipoles but whose electric dipole moments have different magnitudes and effective locations along z axis. Thus, we obtain $m_e \neq 0$ and the original BIC degrades into a Q-BIC that can couple with linearly polarized light along the long axis (x axis) of the nanobars. Correspondingly, the coupling parameter m_e is reduced to

$$m_x \propto p_1(e^{ik\Delta z} - 1) + \Delta p, \quad \Delta p = p_1 - p_2, \quad \Delta z = z_1 - z_2. \quad (3)$$

We calculate the transmission spectra of the WS$_2$ metasurface with the unit cell formed by the pattern II, utilizing the frequency-domain solver in COMSOL Multiphysics 5.6. The periodic boundary conditions are applied in the x and y directions and the perfectly matched layers are used in the z direction. To excite the electric dipole resonance along the long axis of nanobars, the metasurface under the x-linearly polarized incidence (i.e., the incident electric field is oriented along the x axis) is considered. The height of one nanobar is $H_1 = 84$ nm, and that of another is reduced. The dependence of transmission spectra on height differences (ΔH) is shown in Fig. S5(a) of the Supplemental Material [54]. As expected, the BIC resonance is spectrally invisible at $\Delta H = 0$ nm. By reducing the height of one nanobar, i.e., increasing the height difference (ΔH), the radiation channel of the BIC opens and the transmission dip determined by the Q-BIC appears at $\Delta H \neq 0$. Furthermore, the difference in the field enhancement between two nanobars indicates that their electric dipole moments have different magnitudes (see the insets in Fig. S5(b) of the Supplemental Material [54]).

Notably, the Q-BIC with the Q factor exceeding 10^4 is achieved (see Fig. S5(b) of the Supplemental Material [54]). In combination with its strong field enhancement inside the nanobars (see the insets in Fig. S5(b) of the Supplemental Material [54]), we believe that such Q-BIC is conductive to obtain strong light-matter interaction. However, to further achieve photonic spin-dependent light-matter interaction, the chiral Q-BIC is qualified. Here, to realize the chiral Q-BIC, the mirror symmetry of paired parallel nanobars with different heights should be further broken. Specifically, to create a chiral Q-BIC, we consider the metasurface with unit cell formed by the pattern IV where one nanobar is turned on its side and simultaneously both nanobars diverge with the opening angle of θ, as shown in Fig. 1(b). Owing to the two nanobars with equal footprint of $W \times H$ and the length, the supported electric dipoles have same magnitudes ($|\mathbf{p}_1| = |\mathbf{p}_2|$) but different effective z coordinates. The relative displacement of the electric dipole moments along the z axis is roughly estimated by $\Delta z = |H - W|/2$. Meanwhile, the electric dipoles with opposite orientations diverge with the rotation angle of θ. The coupling parameters of the Q-BIC for the right circularly polarized (RCP) and left circularly polarized (LCP) waves can be evaluated by

$$m_{R,L} \propto \sin(\theta \pm k\Delta z/2). \tag{4}$$

Therefore, the metasurface without any point symmetry will allow the supported Q-BIC to possess chirality. To obtain the maximum chiral Q-BIC, we can precisely adjust the diverging angle (θ) to match with the $2\theta = k\Delta z$, where the Q-BIC can strongly interact with the RCP light by $m_R \propto \sin(2\theta)$ and isolate from the LCP light by $m_L = 0$.

The optimized geometric parameters of the metasurface with unit cell formed by the pattern IV are $a = 280$ nm, $L = 155$ nm, $W = 63$ nm, $H = 84$ nm, $D = 140$ nm, and $\theta = 8°$. The Jones matrix of transmission coefficient (t_{mn}) under circular polarization basis is used for characterizing the chiral response [62].

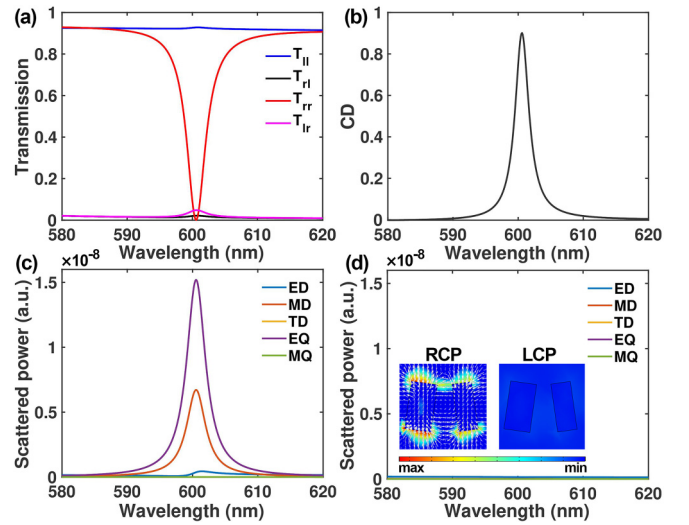$$J_{\mathrm{circ}} = \begin{pmatrix} t_{rr} & t_{rl} \\ t_{lr} & t_{ll} \end{pmatrix}. \tag{5}$$

FIG. 2. (a) Transmission spectra of four Jones matrix elements, corresponding to the metasurface with unit cell formed by the pattern IV. (b) The calculated CD spectrum. (c) and (d) correspond to the scattered power of different multipole moments in the chiral metasurface under RCP and LCP illumination, respectively. The insets in (d) show the electric field distributions of the metasurface unit cell under RCP and LCP illumination, respectively.

Here, the subscripts r and l represent the RCP and LCP, respectively. The t_{mn} ($m = r, l$ and $n = r, l$) stands for the transmission coefficient of output polarization m from input polarization n. The transmission is expressed by $T_{mn} = |t_{mn}|^2$. In the implementation, the circularly polarized light with Jones vectors $\binom{1}{i}$ and $\binom{1}{-i}$ are denoted as LCP and RCP light, respectively. An input port is illuminated with RCP light, and the transmission is monitored at two output ports, specifically measuring T_{rr} and T_{lr}, respectively. Subsequently, the input port is excited by LCP light, and the transmission is monitored at the same two output ports, measuring T_{ll} and T_{rl}, respectively. Transmission spectra of four Jones matrix elements are shown in Fig. 2(a). It is evident that in the absence of cross-polarization transmission contribution, the Q-BIC induces a distinct transmission resonance only for RCP incidence and remains decoupled from LCP incidence. Consequently, the achievement of a chiral Q-BIC is confirmed, and this can be characterized by the circular dichroism (CD). The CD, defined as the transmission difference, is expressed as [63]

$$\mathrm{CD} = \frac{(T_{rr} + T_{lr}) - (T_{ll} + T_{rl})}{(T_{rr} + T_{lr}) + (T_{ll} + T_{rl})}. \tag{6}$$

The calculated CD spectrum is shown in Fig. 2(b), and the maximum CD value reaching 0.91 is obtained at the Q-BIC resonance. In addition, the chiral Q-BIC is verified by the multipole decomposition method [64–67]. The leading multipole moments including electric dipole (ED) moment ($\vec{P}$), magnetic dipole (MD) moment ($\vec{M}$), toroidal dipole (TD) moment ($\vec{T}$), electric quadrupole (EQ) moment ($Q^{(e)}_{\alpha\beta}$), and magnetic quadrupole (MQ) moment ($Q^{(m)}_{\alpha\beta}$) are, respectively,

described by

$$\vec{P} = \frac{1}{i\omega} \int \vec{J} \, d^3 r, \tag{7}$$

$$\vec{M} = \frac{1}{2c} \int (\vec{r} \times \vec{J}) d^3 r, \tag{8}$$

$$\vec{T} = \frac{1}{10c} \int [(\vec{r} \cdot \vec{J}) \vec{r} - 2r^2 \vec{J}] d^3 r, \tag{9}$$

$$\left. \begin{array}{l} Q_{\alpha\beta}^{(e)} = \frac{1}{i\omega} \int \left[r_\alpha J_\beta + r_\beta J_\alpha - \frac{2}{3}(\vec{r} \cdot \vec{J}) \right] d^3 r \\ Q_{\alpha\beta}^{(m)} = \frac{1}{3c} \int [(\vec{r} \times \vec{J})_\alpha r_\beta + (\vec{r} \times \vec{J})_\beta r_\alpha] d^3 r \end{array} \right\} \alpha, \beta = x, y, z. \tag{10}$$

Here, the c is the speed of light in vacuum and ω is angular frequency. The $\vec{r}$ denotes the distance vector from the origin to point (x, y, z) in the Cartesian coordinate. The $\vec{J}$ is the displacement current density within the two WS$_2$ nanobars of a metasurface unit cell. The scattered power from multipole excitation is calculated by

$$I = \frac{2\omega^4}{3c^3} |\vec{P}|^2 + \frac{2\omega^4}{3c^3} |\vec{M}|^2 + \frac{2\omega^6}{3c^5} |\vec{T}|^2 + \frac{\omega^6}{5c^5} \sum |Q_{\alpha\beta}^{(e)}|^2$$
$$+ \frac{\omega^6}{20c^5} \sum |Q_{\alpha\beta}^{(m)}|^2. \tag{11}$$

The scattered power of different multipole moments within the metasurface under RCP and LCP illumination is shown in Figs. 2(c) and 2(d), respectively. The comparison of two figures exhibits that the Q-BIC is dominated by the EQ resonance enabled by a pair of inverted EDs within the unit cell and it is exclusively excited by the RCP light. These results are consistence with the field distributions shown in the insets of Fig. 2(d). The EQ resonance within the unit cell is excited under the RCP incidence, whereas is suppressed at the LCP incidence. Thus, all these findings consistently suggest that the chiral Q-BIC is achieved on the WS$_2$ metasurface with unit cell formed by the pattern IV. This chiral Q-BIC, characterized by an ultrahigh Q factor and strong near-field enhancement on the WS$_2$ metasurface interior, will greatly boost the photon-exciton interaction and further allows the ability to modulate the photon-exciton interaction by simply changing the helicity of the incident light.

To illustrate the potential strong coupling between the Q-BIC resonance and the A exciton in the WS$_2$ metasurface itself, we utilize simulation methods that have been validated by numerous experimental results [25,27,30,41,43]. We tune the wavelength of the Q-BIC resonance across the WS$_2$ A exciton wavelength of 621 nm (2.0 eV) by changing the lengths (L) of two nanobars, because the Q-BIC is driven by the EQ resonance along the long axis of nanobars. Transmission spectra of the pure Q-BIC resonance with different lengths are shown in Figs. 3(a) and 3(b). As expected, the chiral Q-BIC is only excited by the RCP light, as shown in Fig. 3(a). The spectral position of the Q-BIC shows a red shift

as the length (L) increases. When the nanobar length is tuned to $L = 171$ nm, the spectral overlapping between the Q-BIC and the A exciton resonance occurs. Correspondingly, when the A exciton response is considered by setting the oscillator intensity to $f_0 = 0.2$ in the Eq. (1), the typical anticrossing behavior is observed, as shown in Fig. 3(c). The anticrossing behavior near the exciton resonance is the hard evidence of strong coupling between the Q-BIC and the A exciton. As a result, two new branches of self-hybridized exciton-polaritons appear. On the contrary, under the LCP incidence, the Q-BIC is always suppressed and only the transmission dip induced by the A exciton resonance, maintaining unchanged spectral positions at the wavelength of 621 nm, is observed with the increase of the length (L), as shown in Fig. 3(d). Hence,
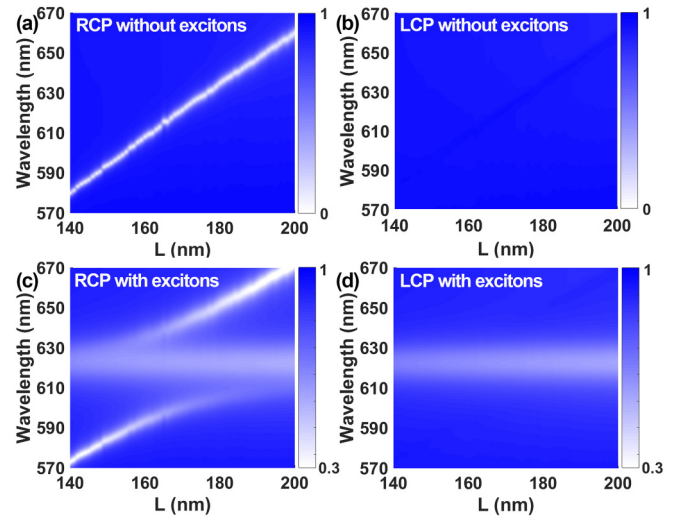

FIG. 3. Transmission spectra of the pure Q-BIC resonance with different lengths of the nanobars under the RCP (a) and LCP (b) illumination. Transmission spectra of the hybrid system as a function of the nanobar length under the RCP (c) and LCP (d) illumination. In (a) and (b), only the background index-only material is considered by setting the oscillator strength to $f_0 = 0$ in the Eq. (1). In (c) and (d), the A exciton response is considered by setting the $f_0 = 0.2$.
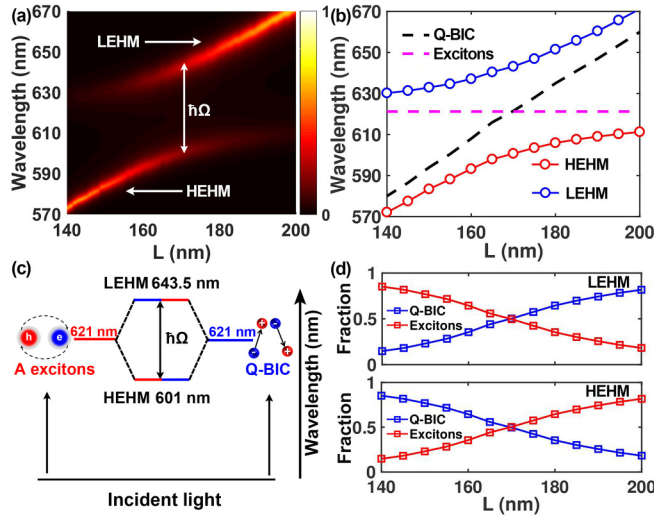
FIG. 4. (a) The CD spectra of the self-hybridized exciton-polaritons. (b) The theoretically calculated wavelengths of two new hybrid states as a function of the nanobar length (L). The black and purple curves represent the intrinsic wavelengths of individual Q-BIC and A excitons, respectively. (c) The energy level diagram at the strong coupling region. (d) Calculated Hopfield coefficients of the LEHM and HEHM, respectively.

we can switch the interaction between the Q-BIC and the A exciton on the WS$_2$ metasurface itself by changing the helicity of the incident light. In other words, based on the chiral Q-BIC resonance, the observed self-hybridized exciton-polaritons are photonic spin dependent.

Based on the Figs. 3(c) and 3(d), the calculated CD spectra are shown in Fig. 4(a). An evident anticrossing behavior with the emergence of two new eigenstates is witnessed. Such behavior can be qualitatively elucidated using the coupled oscillator model in Hamiltonian representation. The satisfied eigenvalue equation is described as [18,68,69]

$$\begin{pmatrix} E_{\text{Q-BIC}} - i\gamma_{\text{Q-BIC}} & g \\ g & E_{\text{exciton}} - i\gamma_{\text{exciton}} \end{pmatrix} \begin{pmatrix} \alpha \\ \beta \end{pmatrix} = E_{\pm} \begin{pmatrix} \alpha \\ \beta \end{pmatrix}. \tag{12}$$

Here, $E_{\text{Q-BIC}}$ and E_{exciton} are the energies of the uncoupled Q-BIC and A excitons, respectively. The $\gamma_{\text{Q-BIC}}$ and γ_{exciton} are the half line widths of the uncoupled Q-BIC and A excitons, respectively. $E_{\pm}$ denote the eigen energies of two new hybrid modes, named by the high- (HEHM) and low-energy (LEHM) hybrid modes, respectively. The g represents the coupling strength between the Q-BIC and A excitons. The α and β are the Hopfield coefficients, which satisfy $|\alpha|^2 + |\beta|^2 = 1$ for the two branches of self-hybridized exciton-polaritons. The mixing fractions of $|\alpha|^2$ and $|\beta|^2$ represent the relative weightings of the Q-BIC and A excitons in the two new hybrid modes, respectively. According to the Eq. (12), the eigenenergies of two new hybrid modes are obtained as

$$E_{\pm} = 0.5(E_{\text{Q-BIC}} + E_{\text{exciton}}) + 0.5i(\gamma_{\text{Q-BIC}} - \gamma_{\text{exciton}})$$

$$\pm \sqrt{g^2 - 0.25[E_{\text{Q-BIC}} - E_{\text{exciton}} + i(\gamma_{\text{Q-BIC}} - \gamma_{\text{exciton}})]^2}. \tag{13}$$

The coupling strength g can be calculated by using the Rabi splitting energy ($\hbar\Omega$) at the detuning of $\delta = E_{\text{Q-BIC}} - E_{\text{exciton}} = 0$, in combination with the half line widths of $\gamma_{\text{Q-BIC}}$ and γ_{exciton}. The coupling strength g thus is determined by

$$g = 0.5\sqrt{\hbar\Omega^2 + i(\gamma_{\text{Q-BIC}} - \gamma_{\text{exciton}})^2}. \tag{14}$$

The Rabi splitting energy of $\hbar\Omega = 137.5$ meV at $\delta = 0$ is extracted from simulation results in Fig. 4(a). Meanwhile, the $\hbar\gamma_{\text{Q-BIC}} = 6.8$ meV is calculated from the transmission spectra in Fig. 3(a), and the $\hbar\gamma_{\text{exciton}} = 25$ meV is obtained from the complex dielectric function of the bulk WS$_2$. The $g = 68.9$ meV thus is obtained by using the Eq. (14). Consequently, the criteria for strong coupling $g > \sqrt{(\gamma_{\text{Q-BIC}}^2 + \gamma_{\text{exciton}}^2)/2}$ is rigorously satisfied. In the strong coupling region of $\delta = 0$, the energy level diagram is illustrated in Fig. 4(c). The two new hybrid modes can be identified as states combining half-Q-BIC and half-exciton characteristics, arising from the strong coupling between Q-BIC and A excitons. The excellent matching between numerical simulations and theoretical results for the energies of hybrid states is also observed in Fig. 4(b). The fractions of the Q-BIC and A exciton constituents in the HEHM and LEHM can be derived from the Eq. (12) and are expressed, respectively, as,

$$|\alpha|^2 = \frac{1}{2}\left(1 \pm \frac{\delta}{\sqrt{\delta^2 + 4g^2}}\right),$$

$$|\beta|^2 = \frac{1}{2}\left(1 \mp \frac{\delta}{\sqrt{\delta^2 + 4g^2}}\right). \tag{15}$$

The fractions of the Q-BIC and A exciton components in the LEHM and HEHM, are demonstrated in Fig. 4(d). As the Q-BIC energy shifts across the A exciton energy from high to low (namely the wavelength gradually increases), the fraction of A excitons decreases at the LEHM, whereas the fraction of the Q-BIC increases. At the HEHM, the opposite behavior yields. Thus, the energy exchange behavior between the Q-BIC and A excitons is confirmed again, which is also the compelling evidence of the anticrossing behavior induced by the strong coupling between the Q-BIC and A excitons. Notably, the values of the fractions of both the Q-BIC and A excitons are close to 0.5 at $\delta = 0$, which indicates the complete formation of a half-light, half-matter hybrid state, as demonstrated in the Fig. 4(c). Finally, it should be pointed out that for the passive WS$_2$ metasurface system, the coupling strength between the Q-BIC and the exciton itself depends on the effective mode volume (V) of the Q-BIC resonance and the exciton transition dipole moment (μ_e), referring to $2g \propto \frac{\mu_e}{\sqrt{V}}$ [70]. In the proposed metasurface, the slight variations in structural parameters minimally affect the effective mode volume of the Q-BIC resonance whose wavelength remains unchanged to match with the exciton wavelength of 621 nm. However, these perturbations may exert a considerable influence on the Q factor of the Q-BIC. As illustrated in Fig. S5(b) of the Supplemental Material [54], the Q factors follow an inverse quadratic relationship with the height difference (ΔH). Consequently, the bandwidth of two branches of exciton-polaritons increases with the height difference (ΔH) increasing (see Fig. S6 of the Supplemental Material [54]).

The exciton transition dipole moment (μ_e) can be characterized by the exciton oscillator strength (f_0). As expected, the Rabi splitting is observed to increase with higher values of f_0, reaching approximately 200 meV at $f_0 = 0.4$ (see Fig. S7 of the Supplemental Material [54]). In addition, considering the practical fabrication of the investigated WS_2 metasurface, the WS_2 flakes can be mechanically exfoliated from bulk crystal using a polydimethylsiloxane stamp and transferred by using the all-dry transfer method [25]. Patterning of the WS_2 flakes can be achieved by utilizing electron beam lithography including the processes such as deposition, patterning, lift-off, and etching.

IV. CONCLUSIONS

In conclusion, we have proposed the chiral Q-BIC scheme to realize the room-temperature self-hybridized excitonic-polaritons on a bulk WS_2 metasurface. Owing to the tight field confinement and ultrahigh Q factor of the Q-BIC, the strong coupling between the Q-BIC and excitons is observed in a compact system composed of an array of paired WS_2 nanobars, without requiring an external microcavity.

The strong-coupling-induced anticrossing behavior, with the Rabi splitting energy up to 136.5 meV, is well illustrated by the coupled oscillator model in Hamiltonian representation. Intriguingly, the chiral Q-BIC with the CD up to 0.91 is achieved on the proposed bulk WS_2 metasurface without any point symmetry. Consequently, photonic-spin-dependent self-hybridized exciton-polaritons are observed. All numerical simulations based on the finite-element method are consistent with the theoretical calculations. The insights gained from this research hold significant promise for the advancement of integrated polaritonic devices. The chiral Q-BIC scheme undoubtedly can serve as a universal recipe for achieving photonic spin-controlled light-matter interactions in bulk semiconductor materials such as TMDs and perovskites.

[1] G. Khitrova, H. M. Gibbs, M. Kira, S. W. Koch, and A. Scherer, Vacuum Rabi splitting in semiconductors, Nat. Phys. **2**, 81 (2006).

[2] S. B. Anantharaman, K. Jo, and D. Jariwala, Exciton-photonics: From fundamental science to applications, ACS Nano **15**, 12628 (2021).

[3] M. Hertzog, M. Wang, J. Mony, and K. Börjesson, Strong light-matter interactions: A new direction within chemistry, Chem. Soc. Rev. **48**, 937 (2019).

[4] F. I. Moxley, E. O. llo-Okeke, S. Mudaliar, and T. Byrnes, Quantum technology applications of exciton-polariton condensates, Emergent Mater. **4**, 971 (2021).

[5] H. Deng, H. Haug, and Y. Yamamoto, Exciton-polariton Bose-Einstein condensation, Rev. Mod. Phys. **82**, 1489 (2010).

[6] A. Imamog, R. J. Ram, S. Pau, and Y. Yamamoto, Nonequilibrium condensates and lasers without inversion: Exciton-polariton lasers, Phys. Rev. A **53**, 4250 (1996).

[7] T. C. H. Liew, A. V. Kavokin, and I. A. Shelykh, Optical circuits based on polariton neurons in semiconductor microcavities, Phys. Rev. Lett. **101**, 016402 (2008).

[8] M. Saba, C. Ciuti, J. Bloch, V. Thierry-Mieg, R. Andre, L. S. Dang, S. Kundermann, A. Mura, G. Bongiovanni, J. L. Staehli, and B. Deveaud, High-temperature ultrafast polariton parametric amplification in semiconductor microcavities, Nature (London) **414**, 731 (2001).

[9] A. I. Tartakovskii, D. N. Krizhanovskii, and V. D. Kulakovskii, Polariton-polariton scattering in semiconductor microcavities: Distinctive features and similarities to the three-dimensional case, Phys. Rev. B **62**, R13298 (2000).

[10] M. Gurioli, J. Martinez-Pastor, M. Colocci, A. Bosacchi, S. Franchi, and L. C. Andreani, Well-width and aluminum-concentration dependence of the exciton binding energies in GaAs/Al$_x$Ga$_{1-x}$As quantum wells, Phys. Rev. B **47**, 15755 (1993).

[11] P. Horodyský and P. Hlídek, Free-exciton absorption in bulk CdTe: Temperature dependence, Phys. Status Solidi Basic Res. **243**, 494 (2006).

[12] S. Ghosh, R. Su, J. Zhao, A. Fieramosca, J. Wu, T. Li, Q. Zhang, F. Li, Z. Chen, T. Liew, D. Sanvitto, and Q. Xiong, Microcavity exciton polaritons at room temperature, Photon. Insights **1**, R04 (2022).

[13] K. F. Mak, C. Lee, J. Hone, J. Shan, and T. F. Heinz, Atomically thin MoS_2: A new direct-gap semiconductor, Phys. Rev. Lett. **105**, 136805 (2010).

[14] A. Chernikov, T. C. Berkelbach, H. M. Hill, A. Rigosi, Y. Li, O. B. Aslan, D. R. Reichman, M. S. Hybertsen, and T. F. Heinz, Exciton binding energy and nonhydrogenic Rydberg series in monolayer WS_2, Phys. Rev. Lett. **113**, 076802 (2014).

[15] A. Raja, A. Chaves, J. Yu, G. Arefe, H. M. Hill, A. F. Rigosi, T. C. Berkelbach, P. Nagler, C. Schüller, T. Korn, C. Nuckolls, J. Hone, L. E. Brus, T. F. Heinz, D. R. Reichman, and A. Chernikov, Coulomb engineering of the bandgap and excitons in two-dimensional materials, Nat. Commun. **8**, 15251 (2017).

[16] L. Zhao, Q. Shang, M. Li, Y. Liang, C. Li, and Q. Zhang, Strong exciton-photon interaction and lasing of two-dimensional transition metal dichalcogenide semiconductors, Nano Res. **14**, 1937 (2021).

[17] T. LaMountain, J. Nelson, E. J. Lenferink, S. H. Amsterdam, A. A. Murthy, H. F. Zeng, T. J. Marks, V. P. Dravid, M. C. Hersam, and N. P. Stern, Valley-selective optical Stark effect of exciton-polaritons in a monolayer semiconductor, Nat. Commun. **12**, 4530 (2021).

[18] X. Liu, T. Galfsky, Z. Sun, F. Xia, E. C. Lin, Y. H. Lee, S. Kéna-Cohen, and V. M. Menon, Strong light-matter coupling in two-dimensional atomic crystals, Nat. Photon. **9**, 30 (2015).

[19] L. Yang, X. Xie, J. Yang, M. Xue, S. Wu, S. Xiao, F. Song, J. Dang, S. Sun, Z. Zou, J. Chen, Y. Huang, X. Zhou, K. Jin, C. Wang, and X. Xu, Strong light-matter interactions between gap plasmons and two-dimensional excitons under ambient conditions in a deterministic way, Nano Lett. **22**, 2177 (2022).

[20] J. Cuadra, D. G. Baranov, M. Wersäll, R. Verre, T. J. Antosiewicz, and T. Shegai, Observation of tunable charged exciton polaritons in hybrid monolayer WS_2-plasmonic nanoantenna system, Nano Lett. **18**, 1777 (2018).

[21] M. Wang, A. Krasnok, T. Zhang, L. Scarabelli, H. Liu, Z. Wu, L. M. Liz-Marzán, M. Terrones, A. Alù, and Y. Zheng, Tunable fano resonance and plasmon-exciton coupling in single au nanotriangles on monolayer WS_2 at room temperature, Adv. Mater. **30**, 1705779 (2018).

[22] W. Du, J. Zhao, W. Zhao, S. Zhang, H. Xu, and Q. Xiong, Ultrafast modulation of exciton-plasmon coupling in a monolayer WS_2-Ag nanodisk hybrid system, ACS Photonics **6**, 2832 (2019).

[23] B. Li, S. Zu, Z. Zhang, L. Zheng, Q. Jiang, B. Du, Y. Luo, Y. Gong, Y. Zhang, F. Lin, B. Shen, X. Zhu, P. M. Ajayan, and Z. Fang, Large Rabi splitting obtained in Ag-WS_2 strong-coupling heterostructure with optical microcavity at room temperature, Opt. Electron. Adv. **2**, 190008 (2019).

[24] Y. Li, A. Chernikov, X. Zhang, A. Rigosi, H. M. Hill, A. M. van der Zande, and T. F. Heinz, Measurement of the optical dielectric function of monolayer transition-metal dichalcogenides: MoS_2, $MoSe_2$, WS_2, and WSe_2, Phys. Rev. B **90**, 205422 (2014).

[25] R. Verre, D. G. Baranov, B. Munkhbat, J. Cuadra, M. Kall, and T. Shegai, Transition metal dichalcogenide nanodisks as high-index dielectric Mie nanoresonators, Nat. Nanotechnol. **14**, 679 (2019).

[26] P. G. Zotev, Y. Wang, L. Sortino, T. Severs Millard, N. Mullin, D. Conteduca, M. Shagar, A. Genco, J. K. Hobbs, T. F. Krauss, and A. I. Tartakovskii, Transition metal dichalcogenide dimer nanoantennas for tailored light-matter interactions, ACS Nano **16**, 6493 (2022).

[27] B. Munkhbat, D. G. Baranov, M. Stührenberg, M. Wersäll, A. Bisht, and T. Shegai, Self-hybridized exciton-polaritons in multilayers of transition metal dichalcogenides for efficient light absorption, ACS Photonics **6**, 139 (2019).

[28] F. Shen, Z. Zhang, Y. Zhou, J. Ma, K. Chen, H. Chen, S. Wang, J. Xu, and Z. Chen, Transition metal dichalcogenide metaphotonic and self-coupled polaritonic platform grown by chemical vapor deposition, Nat. Commun. **13**, 5597 (2022).

[29] M. Nauman, J. Yan, D. de Ceglia, M. Rahmani, K. Z. Kamali, C. De Angelis, A. E. Miroshnichenko, Y. Lu, and D. N. Neshev, Tunable unidirectional nonlinear emission from transition-metal-dichalcogenide metasurfaces, Nat. Commun. **12**, 5597 (2021).

[30] H. Zhang, B. Abhiraman, Q. Zhang, J. Miao, K. Jo, S. Roccasecca, M. W. Knight, A. R. Davoyan, and D. Jariwala, Hybrid exciton-plasmon-polaritons in van der Waals semiconductor gratings, Nat. Commun. **11**, 3552 (2020).

[31] D. Zheng, S. Zhang, Q. Deng, M. Kang, P. Nordlander, and H. Xu, Manipulating coherent plasmon-exciton interaction in a single silver nanorod on monolayer WSe_2, Nano Lett. **17**, 3809 (2017).

[32] K. Koshelev, S. Lepeshov, M. Liu, A. Bogdanov, and Y. Kivshar, Asymmetric metasurfaces with high-Q resonances governed by bound states in the continuum, Phys. Rev. Lett. **121**, 193903 (2018).

[33] M. Kang, S. Zhang, M. Xiao, and H. Xu, Merging bound states in the continuum at off-high symmetry points, Phys. Rev. Lett. **126**, 117402 (2021).

[34] J. Jin, X. Yin, L. Ni, M. Soljačić, B. Zhen, and C. Peng, Topologically enabled ultrahigh-Q guided resonances robust to out-of-plane scattering, Nature (London) **574**, 501 (2019).

[35] R. M. Saadabad, L. Huang, and A. E. Miroshnichenko, Polarization-independent perfect absorber enabled by quasi-bound states in the continuum, Phys. Rev. B **104**, 235405 (2021).

[36] Z. Liu, Y. Xu, Y. Lin, J. Xiang, T. Feng, Q. Cao, J. Li, S. Lan, and J. Liu, High-Q quasibound states in the continuum for nonlinear metasurfaces, Phys. Rev. Lett. **123**, 253901 (2019).

[37] D. R. Abujetas, Á. Barreda, F. Moreno, A. Litman, J. M. Geffrin, and J. A. Sánchez-Gil, High-Q transparency band in all-dielectric metasurfaces induced by a quasi bound state in the continuum, Laser Photon. Rev. **15**, 2000263 (2020).

[38] N. Muhammad, Y. Chen, C. Qiu, and G. Wang, Optical bound states in continuum in MoS_2-based metasurface for directional light emission, Nano Lett. **21**, 967 (2021).

[39] X. Zong, L. Li, and Y. Liu, Photonic bound states in the continuum in nanostructured transition metal dichalcogenides for strong photon-exciton coupling, Opt. Lett. **46**, 6095 (2021).

[40] X. Gu, X. Liu, X. F. Yan, W. J. Du, Q. Lin, L. L. Wang, and G. D. Liu, Polaritonic coherent perfect absorption based on self-hybridization of a quasi-bound state in the continuum and exciton, Opt. Express **31**, 4691 (2023).

[41] M. Qin, J. Duan, S. Xiao, W. Liu, T. Yu, T. Wang, and Q. Liao, Strong coupling between excitons and quasibound states in the continuum in bulk transition metal dichalcogenides, Phys. Rev. B **107**, 045417 (2023).

[42] T. Weber, L. Kühner, L. Sortino, A. B. Mhenni, N. P. Wilson, J. Kühne, J. J. Finley, S. A. Maier, and A. Tittl, Intrinsic strong light-matter coupling with self-hybridized bound states in the continuum in van der Waals metasurfaces, Nat. Mater. **22**, 970 (2023).

[43] P. Xie, Q. Ding, Z. Liang, S. Shen, L. Yue, H. Zhang, and W. Wang, Cavity-assisted boosting of self-hybridization between excitons and photonic bound states in the continuum in multilayers of transition metal dichalcogenides, Phys. Rev. B **107**, 075415 (2023).

[44] Y. Chen, H. Deng, X. Sha, W. Chen, R. Wang, Y. Chen, D. Wu, J. Chu, Y. S. Kivshar, S. Xiao, and C.-W. Qiu, Observation of intrinsic chiral bound states in the continuum, Nature (London) **613**, 474 (2023).

[45] A. Overvig, N. Yu, and A. Alù, Chiral quasi-bound states in the continuum, Phys. Rev. Lett. **126**, 073001 (2021).

[46] H. Li, H. Zhou, G. Wei, H. Xu, M. Qin, J. Liu, and F. Wu, Photonic spin-selective perfect absorptance on planar metasurfaces driven by chiral quasi-bound states in the continuum, Nanoscale **15**, 6636 (2023).

[47] X. Zhang, Y. Liu, J. Han, Y. Kivshar, and Q. Song, Chiral emission from resonant metasurfaces, Science **377**, 1215 (2022).

[48] B. Zhen, C. W. Hsu, L. Lu, A. D. Stone, and M. Soljačić, Topological nature of optical bound states in the continuum, Phys. Rev. Lett. **113**, 257401 (2014).

[49] A. C. Overvig, S. C. Malek, M. J. Carter, S. Shrestha, and N. Yu, Selection rules for quasibound states in the continuum, Phys. Rev. B **102**, 035434 (2020).

[50] Z. Liu, T. Guo, Q. Tan, Z. Hu, Y. Sun, H. Fan, Z. Zhang, Y. Jin, and S. He, Phase interrogation sensor based on all-dielectric BIC metasurface, Nano Lett. **23**, 10441 (2023).

[51] M. V. Gorkunov, A. A. Antonov, V. R. Tuz, A. S. Kupriianov, and Y. S. Kivshar, Bound states in the continuum underpin near-lossless maximum chirality in dielectric metasurfaces, Adv. Opt. Mater. **9**, 2100797 (2021).

[52] M. V. Gorkunov, A. A. Antonov, and Y. S. Kivshar, Metasurfaces with maximum chirality empowered by bound states in the continuum, Phys. Rev. Lett. **125**, 093903 (2020).

[53] Y. Lim, I. C. Seo, S.-C. An, Y. Kim, C. Park, B. H. Woo, S. Kim, H.-R. Park, and Y. C. Jun, Maximally chiral emission via chiral quasibound states in the continuum, Laser Photon. Rev. **17**, 2200611 (2023).

[54] See Supplemental Material at http://link.aps.org/supplemental/10.1103/PhysRevB.109.125201 for the band structure of the metasurface with the unit cell comprising a WS$_2$ nanobar, the band structure of the WS$_2$ metasurface with the unit cell comprising paired parallel and identical nanobars, the dependence of BIC eigenfrequencies on the distance (D) between the centers of nanobars, the radiative Q factors of the BIC band structure for difference distances (D), the transformation of a symmetry-protected BIC into the Q-BIC, the effect of the height difference (ΔH) on the coupling strength, the dependence of the coupling strength on the exciton oscillator strength (f_0).

[55] Q. Liu, L. Qu, Z. Gu, D. Zhang, W. Wu, W. Cai, M. Ren, and J. Xu, Boosting second harmonic generation by merging bound states in the continuum, Phys. Rev. B **107**, 245408 (2023).

[56] H. M. Doeleman, F. Monticone, W. den Hollander, A. Alù, and A. F. Koenderink, Experimental observation of a polarization vortex at an optical bound state in the continuum, Nat. Photon. **12**, 397 (2018).

[57] S. Li, C. Zhou, T. Liu, and S. Xiao, Symmetry-protected bound states in the continuum supported by all-dielectric metasurfaces, Phys. Rev. A **100**, 063803 (2019).

[58] X. Qi, J. Wu, F. Wu, M. Ren, Q. Wei, Y. Wang, H. Jiang, Y. Li, Z. Guo, Y. Yang, W. Zheng, Y. Sun, and H. Chen, Steerable merging bound states in the continuum on a quasi-flatband of photonic crystal slabs without breaking symmetry, Photonics Res. **11**, 1262 (2023).

[59] S. Xiao, M. Qin, J. Duan, F. Wu, and T. Liu, Polarization-controlled dynamically switchable high-harmonic generation

from all-dielectric metasurfaces governed by dual bound states in the continuum, Phys. Rev. B **105**, 195440 (2022).

[60] C. W. Hsu, B. Zhen, A. D. Stone, J. D. Joannopoulos, and M. Soljačić, Bound states in the continuum, Nat. Rev. Mater. **1**, 16048 (2016).

[61] L. Kühner, F. J. Wendisch, A. A. Antonov, J. Bürger, L. Hüttenhofer, L. S. Menezes, S. A. Maier, M. V. Gorkunov, Y. Kivshar, and A. Tittl, Unlocking the out-of-plane dimension for photonic bound states in the continuum to achieve maximum optical chirality, Light: Sci. Appl. **12**, 250 (2023).

[62] C. Menzel, C. Rockstuhl, and F. Lederer, Advanced Jones calculus for the classification of periodic metamaterials, Phys. Rev. A **82**, 053811 (2010).

[63] T. Shi, Z. L. Deng, G. Geng, Y. Zeng, G. Hu, A. Overvig, J. Li, C. W. Qiu, A. Alù, Y. S. Kivshar, and X. Li, Planar chiral metasurfaces with maximal and tunable chiroptical response driven by bound states in the continuum, Nat. Commun. **13**, 4111 (2022).

[64] T. Kaelberer, V. A. Fedotov, N. Papasimakis, D. P. Tsai, and N. I. Zheludev, Toroidal dipolar response in a metamaterial, Science **330**, 1510 (2010).

[65] Y. He, G. Guo, T. Feng, Y. Xu, and A. E. Miroshnichenko, Toroidal dipole bound states in the continuum, Phys. Rev. B **98**, 161112(R) (2018).

[66] P. D. Terekhov, V. E. Babicheva, K. V. Baryshnikova, A. S. Shalin, A. Karabchevsky, and A. B. Evlyukhin, Multipole analysis of dielectric metasurfaces composed of nonspherical nanoparticles and lattice invisibility effect, Phys. Rev. B **99**, 045424 (2019).

[67] H. Li, G. Wei, H. Zhou, H. Xiao, M. Qin, S. Xia, and F. Wu, Polarization-independent near-infrared superabsorption in transition metal dichalcogenide Huygens metasurfaces by degenerate critical coupling, Phys. Rev. B **105**, 165305 (2022).

[68] S. Cao, H. Dong, J. He, E. Forsberg, Y. Jin, and S. He, Normal-incidence-excited strong coupling between excitons and symmetry-protected quasi-bound states in the continuum in silicon nitride-WS$_2$ heterostructures at room temperature, J. Phys. Chem. Lett. **11**, 4631 (2020).

[69] I. A. Al-Ani, K. As' Ham, L. Huang, A. E. Miroshnichenko, W. Lei, and H. T. Hattori, Strong coupling of exciton and high-Q mode in all-perovskite metasurfaces, Adv. Opt. Mater. **10**, 2101120 (2022).

[70] P. Törmä and W. L. Barnes, Strong coupling between surface plasmon polaritons and emitters: A review, Rep. Prog. Phys. **78**, 013901 (2015).